Research article

Guang Yi Jia*, Zhen Xian Huang, Qiao Yun Ma and Geng Li

Photonic spin Hall effect on the surfaces of type-I and type-II Weyl semimetals

https://doi.org/10.1515/nanoph-2019-0468
Received November 15, 2019; revised December 23, 2019; accepted December 27, 2019

Abstract: Topological optics is an emerging research area in which various topological and geometrical ideas are being proposed to design and manipulate the behaviors of photons. Here, the photonic spin Hall effect on the surfaces of topological Weyl semimetal (WSM) films was studied. Our results show that the spin-dependent splitting (i.e. photonic spin Hall shifts) induced by the spin-orbit interaction is little sensitive to the tilt α_t of Weyl nodes and the chemical potential μ in type-I WSM film. In contrast, photonic spin Hall shifts in both the in-plane and transverse directions present versatile dependent behaviors on the α_t and μ in type-II WSM film. In particular, the largest in-plane and transverse spin Hall shifts appear at the tilts between –2 and –3, which are ~40 and ~10 times of the incident wavelength, respectively. Nevertheless, the largest spin Hall shifts for type-II WSM film with positive α_t are only several times of incident wavelength. Moreover, the photonic spin Hall shifts also exhibit different variation trends with decreasing the chemical potential for different signs of α_t in type-II WSM films. This dependence of photonic spin Hall shifts on tilt orientation in type-II WSM films has been explained by time-reversal-symmetry-breaking Hall conductivities in WSMs.

Keywords: photonic spin Hall effect; Weyl semimetal; tilt of Weyl nodes; chemical potential.

***Corresponding author: Guang Yi Jia,** School of Science, Tianjin University of Commerce, Tianjin 300134, P.R. China; and Department of Electrical Engineering, The State University of New York at Buffalo, Buffalo, New York 14260, USA, e-mail: gyjia87@163.com. https://orcid.org/0000-0002-5888-6460
Zhen Xian Huang and Qiao Yun Ma: School of Science, Tianjin University of Commerce, Tianjin 300134, P.R. China
Geng Li: Department of Electrical Engineering, The State University of New York at Buffalo, Buffalo, New York 14260, USA

1 Introduction

Weyl semimetals (WSMs) are the topological phases with broken time-reversal or space-inversion symmetry, whose electronic structure is composed of pairs of Weyl nodes with opposite chirality [1, 2]. They are a prototypical representative of the gapless topological materials, and have been experimentally discovered in three-dimensional condensed matters including $MoTe_2$, WTe_2, NbAs, TaP, TaAs, and so forth [3–6]. WSMs are privileged for many intriguing topographies such as anomalous Hall effect [1, 7], surface states with Fermi arcs [4, 5], large second harmonic generation [2, 8], and circular photogalvanic effect [9, 10], etc. The Weyl nodes in WSMs can be anisotropic and tilted away from the vertical axis [11]. Accordingly, WSMs are classified into type-I (partially tilted) phase with vanishing density of states (DOS) at the Weyl point, and type-II (overtilted) phase with a finite DOS at the Fermi energy and an electron and a hole pocket on either side of the Weyl point [12, 13]. To date, ideal type-I Weyl points with symmetric cone spectra have been ascertained in available semimetals (e.g. NbAs, TaP, TaAs) and also in artificial photonic crystal structures [4–6, 14–16]. In contrast, it was not until 2015 that the concept of type-II WSMs was theoretically proposed by studying the topological properties of WTe_2 and $MoTe_2$ [13, 17]. Even if type-II WSM phase has been experimentally demonstrated in $MoTe_2$, WTe_2, and LaAlGe, among other materials [3, 11, 18–20], many controversial interpretations of the experimental results still exists. In theory, it allows the tilt of two Weyl nodes to be different [11, 21]. Nevertheless, most of the experimentally observed WSMs are oppositely tilted so far [11]. Attempt to search for more type-II WSMs with various tilts is ongoing from both the theoretical and experimental communities [17, 22].

In photoincs, when a polarized Gaussian wave packet is reflected from or transmitted through an interface, its left- and right-circular polarization components will split in directions perpendicular to the refractive index gradient [23, 24]. This phenomenon originates from the spin-orbital interaction (or coupling) and the angular momentum conservation, which is referred to as the photonic spin Hall

effect (PSHE) [23–26]. The PSHE, which is a photonic counterpart of the spin Hall effect in electronic systems, was predicted in theory by Onoda et al. in 2004 and was first confirmed in experiment by Hosten et al. in 2008 [27, 28]. Nowadays, the integration between topological Weyl systems and the PSHE is leading to a burgeoning research interest into hunting for more new and anomalous phenomena in spin-photonics. For instance, Ye et al. recently observed an enhanced PSHE in the vicinity of the Weyl point in a synthetic Weyl system and a helical Zitterbewegung effect when one wave packet traverses very close to the Weyl point [29]. Chen et al. found that the photonic spin Hall shifts on the surface of a WSM thin film was closely related to the distance of Weyl nodes, thus can be utilized to estimate the separation of Weyl nodes in momentum space [30]. Among the research on topological optics, optical conductivity is a key parameter to control and ameliorate the PSHE occurring at a topological interface [30–33]. However, most of the previous studies do not involve the effects of tilt of Weyl nodes and chemical potential on the complex optical conductivity matrices of WSMs for all frequency ranges [12, 33–35]. Therefore, modifying and/or manipulating the PSHE via controlling the tilt and impurity in WSMs, to the best of our knowledge, have not yet been reported so far. The relationship between spin-dependent splitting and the tilt of Weyl nodes (or chemical potential) has remained ambiguous.

In 2019, Sonowal et al. analytically derived the complex optical conductivity matrices of type-I and type-II WSMs as functions of the tilt and chemical potential, which opens up the possibility to solely examine the impacts of tilt α_t of Weyl nodes and chemical potential μ on the PSHE without using any small angle approximation [12]. Besides, the decisive criterion for a type-II WSM is the direct observation of its tilted band crossing in three directions in the momentum space [18]. However, traditional measuring methods including angle-resolved photoemission spectroscopy and scanning tunneling spectroscopy are sometimes invalid to directly observe the tilting Weyl cone and Fermi arcs in WSMs due to their limited resolution [16, 18]. To exploit more flexible and sensitive detection approaches is currently necessary. Motivated by the advances in topological optics, in this work, we theoretically investigated the PSHE on the surfaces of type-I and type-II WSM films by taking into the factors of α_t and μ. Evolutions of in-plane and transverse spin-Hall shifts with α_t and/or μ as well as the possible influencing mechanism are discussed in detail. This work may provide one new strategy to distinguish the topological phases in WSMs.

2 Theoretical model and optical conductivity

As illustrated in Figure 1A, one bulk WSM contains a pair of oppositely tilted Weyl nodes with broken time reversal symmetry [12, 36, 37]. These two Weyl nodes with chirality $\xi = \pm 1$ are located in the Brillouin zone at $\boldsymbol{k} = \{0, 0, \mp Q\}$. The projection of nodes connects the ending points of Fermi arcs on the surfaces of Brillouin zone. The tilt degree of Weyl nodes is expressed by $\alpha_t = v_t / v_F$, with $|\alpha_t| < 1$ being a type-I Weyl node, and $|\alpha_t| > 1$ being a type-II Weyl node. Here, v_t is the tilt velocity of the $\xi = +1$ Weyl node and v_F is the Fermi velocity. According to the Kubo formula, the

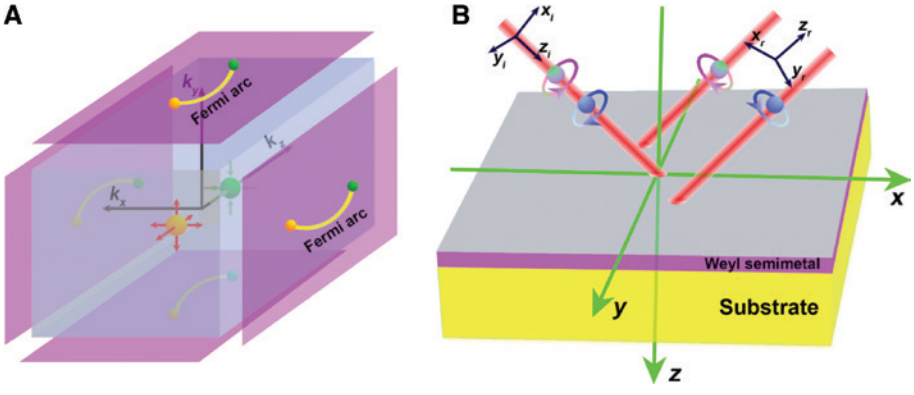

Figure 1: A schematic sketch of the calculation model.
(A) Schematic ***k***-space picture showing a bulk WSM with Fermi arcs on its surface of Brillouin zone. A pair of Weyl nodes along k_z axis are represented by the orange and green pellets with outward arrows as sources and inward arrows as sinks of Berry curvature. Note that surfaces perpendicular to k_z axis do not support arcs. (B) Real-space illustration of the photonic spin splitting of one Gaussian beam reflected from an ultrathin film of WSM. The purple surfaces of WSM host the arc surface states and gray surfaces are ones without arc surface states.

interband optical conductivity of bulk WSM can be written as [12]

$$\sigma_{mn}(\omega)=-\lim_{\gamma\to 0}\sum_{\mathbf{k}}\frac{in_{\mathbf{k}}^{eq}}{\hbar\omega_{\mathbf{k}}}\left[\frac{\left(\mathbf{M}_{\mathbf{k}}^{vc}\otimes\mathbf{M}_{\mathbf{k}}^{cv}\right)_{mn}}{\omega+\omega_{\mathbf{k}}+i\gamma}+\frac{\left(\mathbf{M}_{\mathbf{k}}^{cv}\otimes\mathbf{M}_{\mathbf{k}}^{vc}\right)_{mn}}{\omega-\omega_{\mathbf{k}}+i\gamma}\right] \quad (1)$$

where $m, n\in\{x, y\}$, the parameters of γ, ω and $\hbar\omega_{\mathbf{k}}$ stand for the phenomenological damping factor, angular frequency of incident photons and transition energy, respectively. $n_{\mathbf{k}}^{eq}$ is the equilibrium population difference between the conduction and valance bands, and $\mathbf{M}_{\mathbf{k}}^{vc}=(\mathbf{M}_{\mathbf{k}}^{cv})^{*}$ is the optical matrix element responsible for vertical transition between the valence and conduction bands.

On the basis of Eq. (1), one can deduce that $\sigma_{xx}=\sigma_{yy}$ and $\sigma_{xy}=-\sigma_{yx}$. For simplicity, our model will work in the limit at zero temperature where the Fermi-Dirac distribution function has a Heaviside-step form. Then the real and imaginary parts of the longitudinal conductivity σ_{xx} for a type-I WSM with $|\alpha_t|<1$ are given by

$$\mathrm{Re}(\sigma_{xx})=\begin{cases}0, & \omega<\omega_l\\ \sigma_\omega(1/2-\eta_1), & \omega_l<\omega<\omega_u\\ \sigma_\omega, & \omega>\omega_u\end{cases} \quad (2)$$

$$\mathrm{Im}(\sigma_{xx})=-\frac{\sigma_\omega}{4\pi}\left\{\tau(\alpha_t)\ln\left[\frac{|\omega_u^2-\omega^2|}{|\omega_l^2-\omega^2|}\right]+\frac{8}{\alpha_t^2}\left(\frac{\mu}{\hbar\omega}\right)^2-\left(\frac{\mu}{\hbar\omega}\right)^3\prod(\omega,\alpha_t,\mu)\ln\left[\frac{|\omega_u-\omega|(\omega_l+\omega)}{|\omega_l-\omega|(\omega_u+\omega)}\right]+\frac{6}{|\alpha_t|^3}\left(\frac{\mu}{\hbar\omega}\right)^2\ln\left[\frac{|\omega_u^2-\omega^2|\omega_l^2}{|\omega_l^2-\omega^2|\omega_u^2}\right]+4\ln\left[\frac{|\omega_c^2-\omega^2|}{|\omega_u^2-\omega^2|}\right]\right\} \quad (3)$$

with $\sigma_\omega=e^2\omega/(6\hbar v_F)$, $\hbar\omega_l=2\mu/(1+|\alpha_t|)$, $\hbar\omega_u=2\mu/(1-|\alpha_t|)$ and

$$\eta_1=\frac{3}{8|\alpha_t|}\left(\frac{2\mu}{\hbar\omega}-1\right)\left[1+\frac{1}{3\alpha_t^2}\left(\frac{2\mu}{\hbar\omega}-1\right)^2\right] \quad (4)$$

$$\tau(\alpha_t)=\frac{1}{2}\left(4+\frac{1}{|\alpha_t|^3}+\frac{3}{|\alpha_t|}\right) \quad (5)$$

$$\prod(\omega,\alpha_t,\mu)=\frac{4}{|\alpha_t|^3}+3\left(\frac{\hbar\omega}{\mu}\right)^2\left(\frac{1}{|\alpha_t|^3}+\frac{1}{|\alpha_t|}\right) \quad (6)$$

In the above equations, μ is the chemical potential and $\omega_c\equiv v_F k_c$ is the ultraviolet cutoff frequency. For a type-II WSM with $|\alpha_t|>1$, we have

$$\mathrm{Re}(\sigma_{xx})=\begin{cases}0, & \omega<\omega_l\\ \sigma_\omega(1/2-\eta_1), & \omega_l<\omega<\omega_u'\\ \sigma_\omega\eta_2, & \omega>\omega_u'\end{cases} \quad (7)$$

$$\mathrm{Im}(\sigma_{xx})=-\frac{\sigma_\omega}{4\pi}\left\{\tau(\alpha_t)\ln\left[\frac{|\omega_u'^2-\omega^2|}{|\omega_l^2-\omega^2|}\right]+\frac{8}{\alpha_t^3}\left(\frac{\mu}{\hbar\omega}\right)^2-\left(\frac{\mu}{\hbar\omega}\right)^3\prod(\omega,\alpha_t,\mu)\ln\left[\frac{|\omega_u'-\omega|(\omega_l+\omega)}{|\omega_l-\omega|(\omega_u'+\omega)}\right]+\frac{6}{|\alpha_t|^3}\left(\frac{\mu}{\hbar\omega}\right)^2\ln\left[\frac{|\omega_u'^2-\omega^2|\omega_l^2}{|\omega_l^2-\omega^2|\omega_u'^2}\right]+\left(\frac{3}{|\alpha_t|}+\frac{1}{|\alpha_t|^3}\right)\ln\left[\frac{|\omega_c^2-\omega^2|}{|\omega_u'^2-\omega^2|}\right]+\frac{12}{|\alpha_t|^3}\left(\frac{\mu}{\hbar\omega}\right)^2\ln\left[\frac{|\omega_c^2-\omega^2|\omega_u'^2}{|\omega_u'^2-\omega^2|\omega_c^2}\right]\right\} \quad (8)$$

with $\hbar\omega_u'=2\mu/(|\alpha_t|-1)$ and

$$\eta_2=\frac{3}{4|\alpha_t|}\left[1+\frac{1}{3\alpha_t^2}+\left(\frac{2\mu}{\alpha_t\hbar\omega}\right)^2\right] \quad (9)$$

The Weyl nodes in a WSM can be viewed as a source or sink of the Berry curvature, which acts as a magnetic field in the momentum space. This finite Berry phase permits nontrivial band topology which can induce an anomalous Hall effect and contributes to the anomalous conductivity [7, 12, 38]. In the cases of type-I and II WSMs, the components of anomalous Hall conductivity are given by

$$\sigma_{xy}^{\text{anom-I}}=\sigma_Q+\sigma_\mu\left[\frac{2}{\alpha_t}+\frac{1}{\alpha_t^2}\ln\left(\frac{1-\alpha_t}{1+\alpha_t}\right)\right] \quad (10)$$

$$\sigma_{xy}^{\text{anom-II}}=\frac{\sigma_Q}{|\alpha_t|}+\frac{\mathrm{sgn}(\alpha_t)\sigma_\mu}{\alpha_t^2}\ln\left[\frac{\mu^2}{\hbar^2\omega_c^2\alpha_t^2(\alpha_t^2-1)}\right] \quad (11)$$

respectively. Thus, the off-diagonal Hall conductivity $\sigma_{xy}(\omega)$ including its real and imaginary parts for a type-I WSM with $|\alpha_t|<1$ can be calculated by

$$\mathrm{Re}(\sigma_{xy})=\sigma_{xy}^{\text{anom-I}}+\mathrm{sgn}(\alpha_t)\sigma_\mu\left\{\frac{-1}{2\alpha_t^2}\ln\left[\frac{|\omega_u^2-\omega^2|\omega_l^2}{|\omega_l^2-\omega^2|\omega_u^2}\right]+\left(\frac{\mu}{2\hbar\omega\alpha_t^2}+\frac{\hbar\omega}{8\mu}\frac{1-\alpha_t^2}{\alpha_t^2}\right)\ln\left[\frac{|\omega_u-\omega|(\omega_l+\omega)}{|\omega_l-\omega|(\omega_u+\omega)}\right]-\frac{1}{|\alpha_t|}\right\} \quad (12)$$

$$\mathrm{Im}(\sigma_{xy})=\mathrm{sgn}(\alpha_t)\begin{cases}0, & \omega<\omega_l\\ 3\sigma_\omega\eta_3, & \omega_l<\omega<\omega_u\\ 0, & \omega>\omega_u\end{cases} \quad (13)$$

with $\sigma_\mu = e^2\mu/(h^2 v_F)$, $\sigma_Q = e^2 Q/(\pi h)$, and

$$\eta_3 = \frac{1}{\alpha_t^2}\left(\frac{1}{8} - \frac{\mu}{2\hbar\omega} + \frac{\mu^2}{2\hbar^2\omega^2}\right) - \frac{1}{8} \tag{14}$$

For a type-II WSM with $|\alpha_t| > 1$, we have

$$\mathrm{Re}(\sigma_{xy}) = \sigma_{xy}^{\text{anom-II}} + \mathrm{sgn}(\alpha_t)\sigma_\mu \left\{ \frac{-1}{2\alpha_t^2} \ln\left[\frac{(\omega_c^2-\omega^2)^2 \omega_l^2 \omega_u'^2}{|\omega_l^2-\omega^2||\omega_u'^2-\omega^2|\omega_c^4} \right] + \left(\frac{\mu}{2\hbar\omega\alpha_t^2} + \frac{\hbar\omega}{8\mu}\frac{1-\alpha_t^2}{\alpha_t^2} \right) \ln\left[\frac{|\omega_u'-\omega|(\omega_l+\omega)}{|\omega_l-\omega|(\omega_u'+\omega)} \right] - \frac{2}{\alpha_t^2} \right\} \tag{15}$$

$$\mathrm{Im}(\sigma_{xy}) = \mathrm{sgn}(\alpha_t) \begin{cases} 0, & \omega < \omega_l \\ 3\sigma_\omega \eta_3, & \omega_l < \omega < \omega_u' \\ \dfrac{-3\mu\sigma_\omega}{\hbar\omega\alpha_t^2}, & \omega > \omega_u' \end{cases} \tag{16}$$

We considered an ultrathin WSM film whose thickness d is much smaller than the wavelength λ_0 of incident photons while being larger than the atomic separation a, i.e. $a << d << \lambda_0$. In this limit, the ultrathin WSM can be treated as a 2D atomic layer when it interacts with incident photons [12, 30, 36]. And the surface conductivity of 2D WSM depositing upon a homogeneous substrate can be approximated as $\sigma_{mns} = d\sigma_{mn}$ [12, 30, 36]. The nontrivial properties of 2D WSM enter only through the boundary condition for electromagnetic fields into two non-topological media on either side [36]. Here, the parameters of $\lambda_0 = 632.8$ nm, $d = 10$ nm and $v_F = 1\times10^6$ m/s are chosen. The Weyl node separation is set as $Q = 3.2\times10^8$ m^{-1} which is at the scale of Q in both type-I and II WSMs and matching with that value in WTe_2 [18, 38].

Figure 2A, B describe the relative orientation of a pair of Weyl nodes for $\alpha_t > 0$ and for $\alpha_t < 0$, respectively. The complex optical conductivities σ_{xxs} and σ_{xys} as a function of tilt α_t are shown in Figure 2C and D. It is seen that both σ_{xxs} and σ_{xys} of type-I WSM film ($|\alpha_t| < 1$) are less dependent upon the tilt α_t and the ratio $\hbar\omega/\mu$. This could imply that doping has little effect on the conductivity of type-I WSM film for a certain frequency. For type-II WSM film ($|\alpha_t| > 1$), the absolute value of $\mathrm{Re}(\sigma_{xxs})$ or $\mathrm{Im}(\sigma_{xxs})$ gradually decreases with increasing $|\alpha_t|$ while being nearly not affected by $\hbar\omega/\mu$. As for the Hall conductivity σ_{xys} of type-II WSM film, it is sensitive to both α_t and $\hbar\omega/\mu$. In order to more clearly reveal the evolution of optical conductivity with the ratio $\hbar\omega/\mu$, Figure S1 in the Supplementary Material presents the complex optical conductivities of σ_{xxs} and σ_{xys} as a function of $\hbar\omega/\mu$ for WSM films with $\alpha_t = \pm 2.5$. It further corroborates that the ratio $\hbar\omega/\mu$ has little effect on the longitudinal conductivity σ_{xxs} (the difference induced by changing $\hbar\omega/\mu$ is smaller than $0.0025\sigma_0$). Nevertheless, the function curves of Hall conductivity σ_{xys} for type-II WSM films with $\pm\alpha_t$ are nearly symmetrically varied with

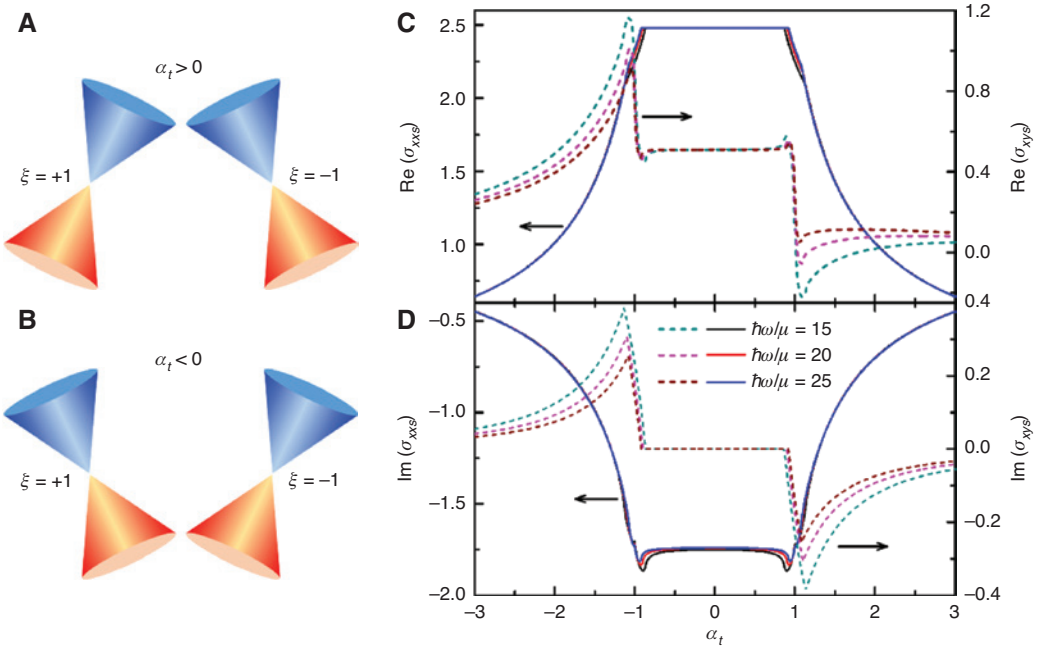

Figure 2: Tilted Weyl nodes and optical conductivity spectra.
Tilted conical spectra of a pair of Weyl nodes for (A) $\alpha_t > 0$ and (B) $\alpha_t < 0$. (C) Real and (D) imaginary parts of optical conductivities σ_{xxs} (solid lines) and σ_{xys} (dashed lines). The conductivities are all scaled in the unit of $\sigma_0 = 2e^2/h$.

increasing the ratio $\hbar\omega/\mu$. In the following Section, we will show that the diversity of optical conductivity of WSM films gives rise to versatile behaviors of photonic spin Hall shifts.

In additon, to verify the accuracy of our calculations, Figure S2 in the Supplementary Material gives the variations of σ_{xxs} and σ_{xys} with different α_t and $\hbar\omega/\mu$ values for a certain chemical potential $\mu = 0.021$ eV, in which the conductivity spectrum of σ_{xys} has ever been reported in [12]. One can see that the real part of Hall conductivity σ_{xys} is less sensitive to the photonic energy. However, the σ_{xxs} as well as the imaginary part of σ_{xys} is sensitive to the changes of both α_t and $\hbar\omega/\mu$ if the frequency of incident photons is large enough. They are well in line with the results in [12]. In this work, we have mainly focused on the PSHE when the incident wavelength is 632.8 nm. Influences of different photonic energies on the PSHE for a certain chemical potential will be studied elsewhere. All the numerical calculation is performed in MATLAB R2019a.

3 Photonic spin Hall shifts

We posit that one Gaussian beam is illuminated on the surface of ultrathin WSM film without Fermi arc states, as depicted in Figure 1B. The incident plane of light lies in the x-z plane of laboratory Cartesian coordinate (x, y, z). Besides, we utilized the coordinate frames (x_i, y_i, z_i) and (x_r, y_r, z_r) to signify the central wave vectors of incident and reflected wave packets, respectively. By solving the electromagnetic boundary conditions on either side of the thin film, the Fresnel reflection coefficients of WSM-substrate are expressed as functions of complex conductivity of WSM film [12]

$$r_{pp} = -1 + \frac{2}{c_0\mu_0}\left[\frac{\sigma_{1s}\cos\theta_t}{\sigma_{1s}\sigma_{2s} - \sigma_{xys}\sigma_{yxs}\cos\theta_i\cos\theta_t}\right] \tag{17a}$$

$$r_{ss} = -1 + \frac{2}{c_0\mu_0}\left[\frac{\sigma_{2s}\cos\theta_i}{\sigma_{1s}\sigma_{2s} - \sigma_{xys}\sigma_{yxs}\cos\theta_i\cos\theta_t}\right] \tag{17b}$$

$$r_{ps} = \frac{2}{c_0\mu_0}\frac{\sigma_{yxs}\cos\theta_i\cos\theta_t}{\sigma_{xys}\sigma_{yxs}\cos\theta_i\cos\theta_t - \sigma_{1s}\sigma_{2s}} \tag{17c}$$

$$r_{sp} = \frac{2}{c_0\mu_0}\frac{\sigma_{xys}\cos\theta_i\cos\theta_t}{\sigma_{xys}\sigma_{yxs}\cos\theta_i\cos\theta_t - \sigma_{1s}\sigma_{2s}} \tag{17d}$$

where $\sigma_{1s} \equiv \cos\theta_i/(c_0\mu_0) + n_t\cos\theta_t/(c_0\mu_0) + \sigma_{xxs}$ and $\sigma_{2s} \equiv \cos\theta_t/(c_0\mu_0) + n_t\cos\theta_i/(c_0\mu_0) + \sigma_{yys}\cos\theta_i\cos\theta_t$. Here, the parameters of c_0, μ_0, θ_i and θ_t are the velocity of light in vacuum, vacuum permeability, incident and refraction angles, respectively. The refractive index n_t of substrate are set as 1.46, coinciding with that value of amorphous SiO_2 substrate at visible light.

It is assumed that the angular spectrum of the incident Gaussian beam in momentum space is specified by $|\Phi\rangle = w_0/\sqrt{2\pi}\exp[-w_0^2(k_{ix}^2 + k_{iy}^2)/4]$ where w_0 is the width of wave function. For horizontal $|H(k_i)\rangle$ and vertical $|V(k_i)\rangle$ polarization states of photons incident upon the surface of WSM thin film, after reflection, the polarization states of wave packets are determined by [30]

$$\begin{pmatrix} |H(k_r)\rangle \\ |V(k_r)\rangle \end{pmatrix} = \begin{pmatrix} r_{pp} - \dfrac{k_{ry}(r_{ps} - r_{sp})\cot\theta_i}{k_0} & r_{ps} + \dfrac{k_{ry}(r_{pp} + r_{ss})\cot\theta_i}{k_0} \\ r_{sp} - \dfrac{k_{ry}(r_{pp} + r_{ss})\cot\theta_i}{k_0} & r_{ss} - \dfrac{k_{ry}(r_{ps} - r_{sp})\cot\theta_i}{k_0} \end{pmatrix} \begin{pmatrix} |H(k_i)\rangle \\ |V(k_i)\rangle \end{pmatrix} \tag{18}$$

where k_0 is the wave vector in vacuum, k_{ix} and k_{iy} (k_{rx} and k_{ry}) represent the wave-vector components of incident (reflected) beam along x_i and y_i (x_r and y_r) axes, respectively. According to the boundary conditions, $k_{rx} = -k_{ix}$ and $k_{ry} = k_{iy}$. In the spin basis set, linearly polarized states of $|H\rangle$ and $|V\rangle$ are decomposed into two orthogonal spin components

$$|H\rangle = (|+\rangle + |-\rangle)/\sqrt{2} \tag{19a}$$

$$|V\rangle = i(|-\rangle - |+\rangle)/\sqrt{2} \tag{19b}$$

where $|+\rangle$ and $|-\rangle$ stand for the left- and right-circular polarization components, respectively.

Under the paraxial approximation, spin-dependent Hall shifts of these two orthogonal components in reflected beam can be mathematically derived according to Eqs. (17)–(19). For simplicity, incident photons are assumed to be only horizontally polarized in this work. The corresponding in-plane and transverse spin Hall shifts for left- and right-circular polarization components, as indicated in Figure 1B, are given by [30, 39]

$$\langle\Delta x_\pm\rangle = \mp\frac{1}{k_0}\mathrm{Re}\left(\frac{r_{pp}}{r_{pp}^2 + r_{sp}^2}\frac{\partial r_{sp}}{\partial\theta_i} - \frac{r_{sp}}{r_{pp}^2 + r_{sp}^2}\frac{\partial r_{pp}}{\partial\theta_i}\right) \tag{20}$$

$$\langle\Delta y_\pm\rangle = \mp\frac{\cot\theta_i}{k_0}\mathrm{Re}\left(\frac{r_{pp} + r_{ss}}{r_{pp}^2 + r_{sp}^2}r_{pp} - \frac{r_{ps} - r_{sp}}{r_{pp}^2 + r_{sp}^2}r_{sp}\right) \tag{21}$$

Figure 3 shows the variations of in-plane and transverse spin Hall shifts (i.e. $\langle\Delta x_+\rangle$ and $\langle\Delta y_+\rangle$) for the

left-circular component with respect to the tilt α_t and the incident angle when $\mu = 0.125$ eV. The colorbars including those appearing in Figures 4 and 5 are all scaled in the unit of λ_0. Previous studies have demonstrated that the spin Hall shifts are sensitive to the minimum values of $|r_{pp}|$ such that they generally give extreme values around the Brewster's angles [39, 40]. This change tendency is reproduced through comparing Figure 3 with Figure S3 in the Supplementary Material. It is found that the Brewster's angle for type-I WSM film ($|\alpha_t| < 1$) appears at about 57.5°, and the maximum values of $\langle \Delta x_+ \rangle$ and $\langle \Delta y_+ \rangle$ are $2.65\lambda_0$ and $1.40\lambda_0$, respectively. As the tilt $|\alpha_t|$

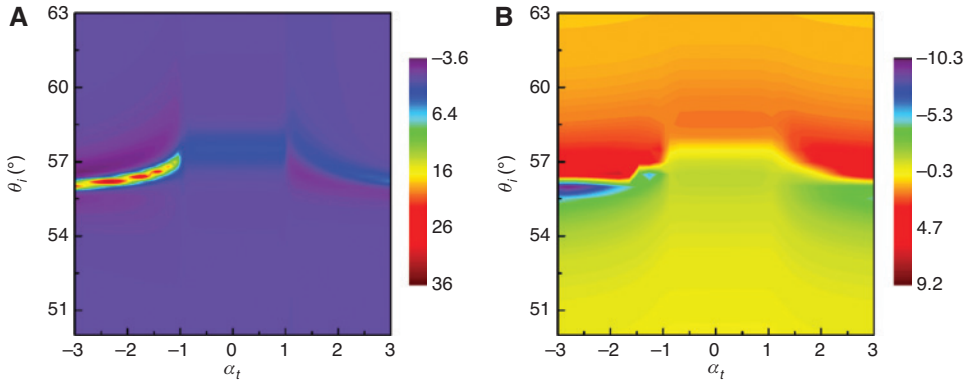

Figure 3: Influences of the tilt α_t and the incident angle on the photonic spin Hall shifts.
(A) In-plane and (B) transverse spin Hall shifts ($\langle \Delta x_+ \rangle$ and $\langle \Delta y_+ \rangle$) as a function of the tilt α_t and the incident angle when $\mu = 0.125$ eV.

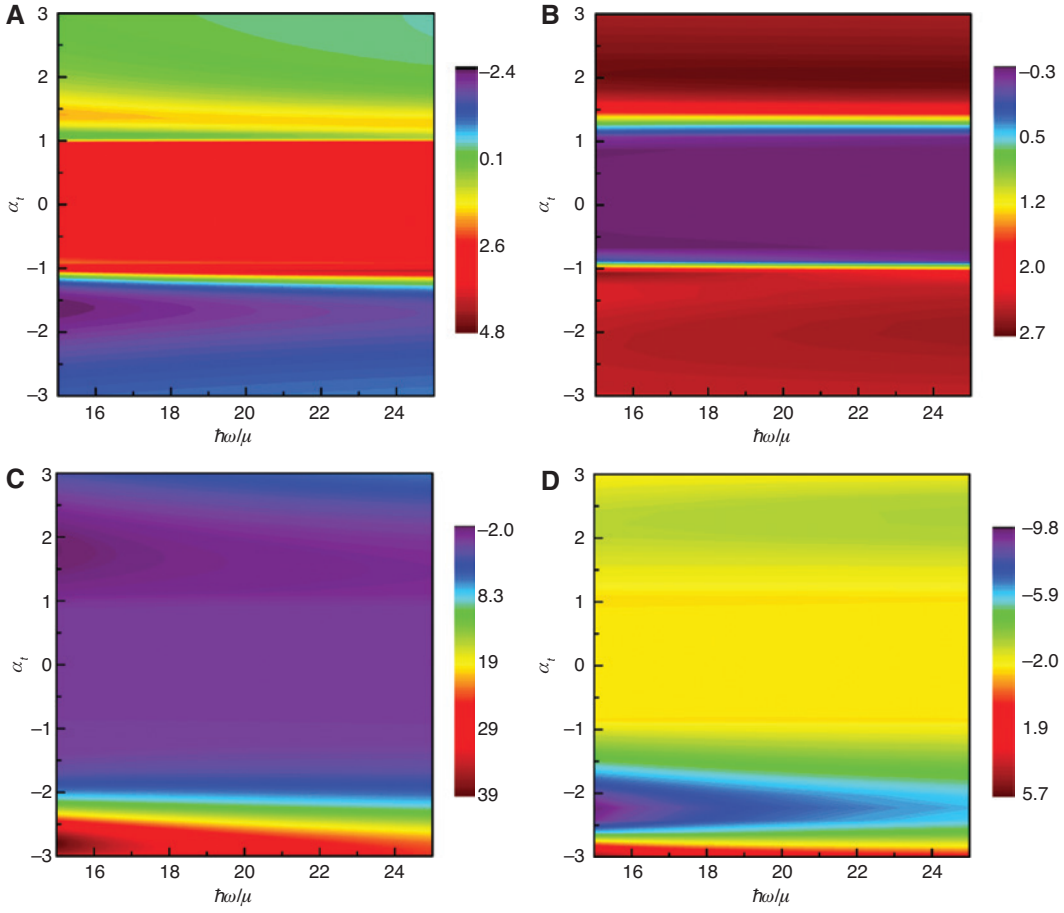

Figure 4: Influences of the tilt α_t and $\hbar\omega/\mu$ on the photonic spin Hall shifts.
(A), (C) In-plane and (B), (D) transverse spin Hall shifts as a function of the tilt α_t and $\hbar\omega/\mu$. The incident angles for (A), (B) and (C), (D) are $\theta_i = 57.5°$ and 56.1°, respectively.

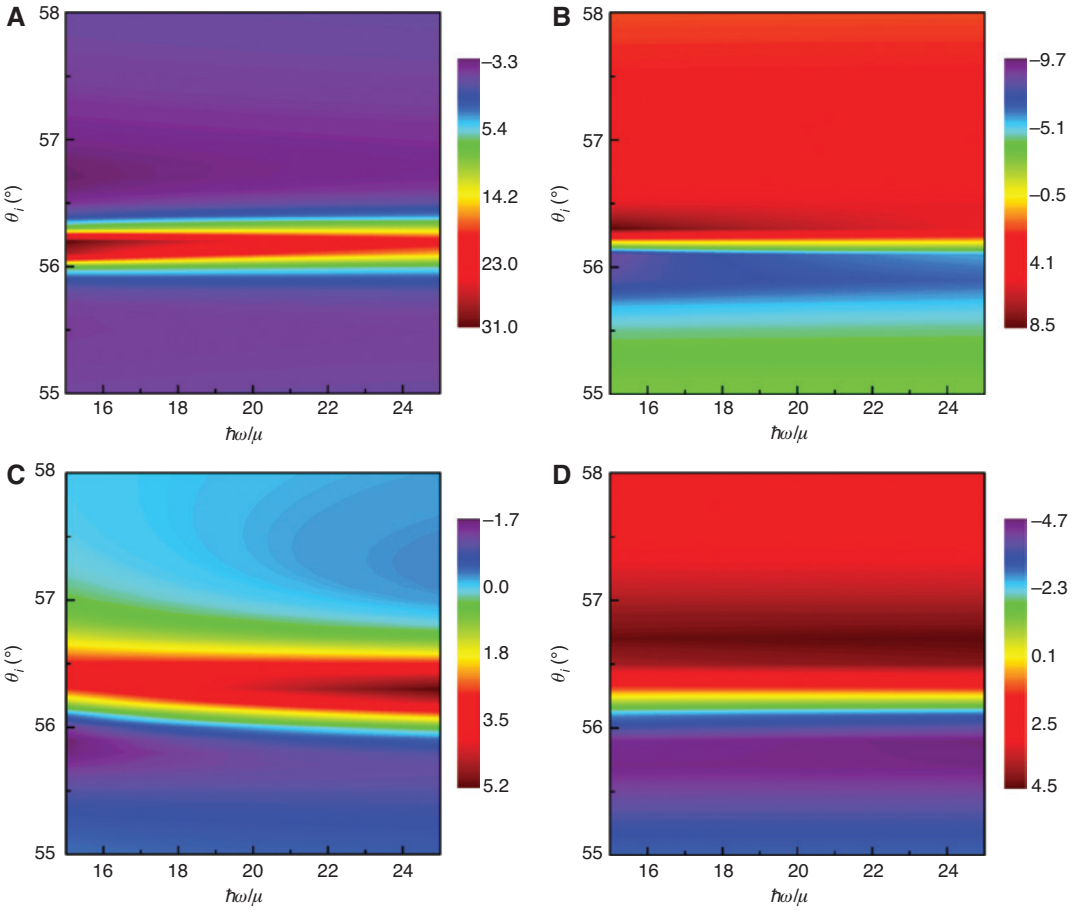

Figure 5: Influences of the incident angle and $\hbar\omega/\mu$ on the photonic spin Hall shifts.
(A), (C) In-plane and (B), (D) transverse spin Hall shifts as a function of the incident angle and $\hbar\omega/\mu$. The tilts for (A), (B) and (C), (D) are $\alpha_t = -2.5$ and 2.5, respectively.

increases from 1 to 3 (type-II WSM film), the Brewster's angle decreases from ~57.5° to 56.1° (see Figure S3 in the Supplementary Material), and the maximum absolute values of $\langle\Delta x_+\rangle$ ($36.31\lambda_0$) and $\langle\Delta y_+\rangle$ ($-10.25\lambda_0$) occur around $\alpha_t = -2.82$ with $\theta_i = 56.1°$.

Figure 4 presents the in-plane and transverse spin Hall shifts as a function of the tilt α_t and $\hbar\omega/\mu$ at Brewster's angles of type-I (A, B) and type-II (C, D) WSM films. We can see that the spin Hall shifts with $|\alpha_t| < 1$ are relatively flat and have a similar variation tendency with the optical conductivity of type-I WSM film (see Figure 2). Thus both $\langle\Delta x_+\rangle$ and $\langle\Delta y_+\rangle$ are less sensitive to the variance of tilt α_t and chemical potential μ. And the in-plane and transverse spin Hall shifts for type-I WSM film in Figure 4A and B are about $2.66\lambda_0$ and $-0.25\lambda_0$, respectively. As for the thin film of type-II WSM with $|\alpha_t| > 1$, the maximum spin Hall shifts in the in-plane and transverse directions are $\langle\Delta x_+\rangle = 38.47\lambda_0$ and $\langle\Delta y_+\rangle = -9.79\lambda_0$. Their corresponding tilts are $\alpha_t = -2.80$ and –2.31, respectively, and both the in-plane and transverse spin Hall shifts gradually decrease as the chemical potential (or $\hbar\omega/\mu$) decreases (or increases), as shown in Figure 4C and D.

From Figures 3 and 4, we drew a conclusion that the maximum spin Hall shifts in both in-plane and transverse directions favor emerging at the tilts between –2 and –3. In view of this, Figure 5A and B exhibit the in-plane and transverse spin Hall shifts as a function of the incident angle and $\hbar\omega/\mu$ with $\alpha_t = -2.5$. For comparison, corresponding spin Hall shifts with $\alpha_t = 2.5$ are also shown in Figure 5C and D. It is seen that the largest in-plane spin Hall shift with $\alpha_t = -2.5$ is $30.95\lambda_0$ which appears at $\theta_i = 56.2°$ (Figure 5A). At incident angles being a little larger and smaller than 56.2°, the sign of transverse spin Hall shift changes from positive to negative (Figure 5B). And the spin Hall shifts in both in-plane and transverse directions gradually decrease with the reducing (or increasing) of chemical potential (or $\hbar\omega/\mu$) for a fixed incident angle.

In marked contrast, the maximum spin Hall shifts in the in-plane and transverse directions for WSM film with $\alpha_t = 2.5$ are only several times of incident wavelength (see

Figure 5C and D). Besides, the in-plane spin Hall shift at incident angles near 56.3° gradually increases as the chemical potential decreases, exhibiting an inverse variation trend comparing with that $\langle \Delta x_+ \rangle$ in Figure 5A. To further confirm these differences between type-II WSM films with different signs of α_t, photonic spin Hall shifts $\langle \Delta x_+ \rangle$ and $\langle \Delta y_+ \rangle$ as functions of the incident angle and $\hbar\omega/\mu$ for type-II WSM films with $\alpha_t = \pm 1.5$ (see Figure S4) and $\alpha_t = \pm 3.0$ (see Figure S5) are also shown in the Supplementary Material. They demonstrate that the maximum $\langle \Delta x_+ \rangle$ (or $\langle \Delta y_+ \rangle$) value of negtive α_t is larger than that of positive α_t. For a fixed incident angle, photonic spin Hall shifts at negative α_t mainly show a decreasing tendency with reducing the chemical potential while the in-plane spin Hall shift at positive α_t may gradually increase as the chemical potential decreases.

These different behaviors in PSHE between type-II WSM films with $\pm\alpha_t$ might be attributed to different dependences of optical Hall conductivity σ_{xys} on the ratio $\hbar\omega/\mu$ induced by reversing the sign of α_t. In general, a finite Hall conductivity of WSM stems from the breaking of the time-reversal symmetry. This manifests in the separation of two Weyl nodes with opposite chirality in the momentum space [11, 12]. As a result, the real part of σ_{xys} with negative α_t is monotonically decreased while that with positive α_t is monotonically increased as the $\hbar\omega/\mu$ increases, as shown in Figure S1B in the Supplementary Material. Besides, the imaginary part of σ_{xys} reverses its sign upon changing the tilt orientation ($\alpha_t \to -\alpha_t$). As for the longitudinal conductivity σ_{xx}, as mentioned above, it is less sensitive to the sign of α_t and the ratio $\hbar\omega/\mu$. More specifically, the $\mathrm{Re}(\sigma_{xxs})$ values are exactly the same, and the largest difference between the $\mathrm{Im}(\sigma_{xxs})$ values is only $\sim 9\times10^{-4}\sigma_0$ for WSM films with $\alpha_t = \pm 2.5$ (see Figure S1A in the Supplementary Material). Therefore, different behaviors of spin Hall shifts for opposite tilt orientations could be ascribed to the remarkable discrepancy in optical Hall conductivities induced by the broken time reversal symmetry in type-II WSM thin films.

4 Conclusions

In summary, the spin-dependent splitting induced by the spin-orbit interaction is investigated in detail, when one linearly polarized light is incident upon the WSM surface without Fermi arc states. We show that the photonic spin Hall shifts on the surface of type-I WSM film are little sensitive to the variance of tilt α_t and chemical potential μ due to the weak susceptibility of optical conductivity to α_t and μ. By contrast, both the in-plane and transverse photonic spin Hall shifts on the surface of type-II WSM film present versatile dependent behaviors on the tilt orientation and the chemical potential. In particular, the maximum spin Hall shifts appear at the tilts between –2 and –3, and the largest values of available $\langle \Delta x_+ \rangle$ and $\langle \Delta y_+ \rangle$ are ~40 and ~10 times of incident wavelength, respectively. Nonetheless, the maximum spin Hall shifts for type-II WSM film with positive α_t are only several times of incident wavelength. Moreover, the photonic spin Hall shifts at negative α_t mainly show a decreasing tendency with reducing the chemical potential, however, the in-plane spin Hall shift at positive α_t gradually increases as the chemical potential decreases at some special incident angles. This dependence of photonic spin Hall shifts on tilt orientation may arise from the striking differences in optical Hall conductivities induced by the broken time reversal symmetry in type-II WSM thin films. In consequence, measuring the photonic spin Hall shifts may provide an alternative way to determine the types of WSMs. These findings may also open up new opportunities to investigate and characterize the doping and the tilt orientation of Weyl nodes in WSMs.

Acknowledgements: The authors acknowledge the National Natural Science Foundation of China (No. 11804251) and the program of study abroad for young scholar sponsored by TJCU for financial support.

References

[1] Ma Q, Xu SY, Shen H, et al. Observation of the nonlinear Hall effect under time-reversal-symmetric conditions. Nature 2019;565:337–42.
[2] Weng H. Lighting up Weyl semimetals. Nat Mater 2019;18:428–34.
[3] Kimura S, Nakajima Y, Mita Z, et al. Optical evidence of the type-II Weyl semimetals $MoTe_2$ and WTe_2. Phys Rev B 2019;99:195203.
[4] Yang HF, Yang LX, Liu ZK, et al. Topological Lifshitz transitions and Fermi arc manipulation in Weyl semimetal NbAs. Nat Commun 2019;10:3478.
[5] Min CH, Bentmann H, Neu JN, et al. Orbital fingerprint of topological Fermi arcs in the Weyl semimetal TaP. Phys Rev Lett 2019;122:116402.
[6] Zhang CL, Wang CM, Yuan Z, et al. Non-saturating quantum magnetization in Weyl semimetal TaAs. Nat Commun 2019;10:1028.
[7] Acheche S, Nourafkan R, Tremblay A-MS. Orbital magnetization and anomalous Hall effect in interacting Weyl semimetals. Phys Rev B 2019;99:075144.
[8] Li Z, Jin Y-Q, Tohyama T, Iitaka T, Zhang J-X, Su H. Second harmonic generation in the Weyl semimetal TaAs from a quantum kinetic equation. Phys Rev B 2018;97:085201.
[9] Ji Z, Liu G, Addison Z. Spatially dispersive circular photogalvanic effect in a Weyl semimetal. Nat Mater 2019;18:955–62.

[10] Hotz F, Tiwari A, Turker O, et al. Exactly soluble model for a fractionalized Weyl semimetal. Phys Rev Res 2019;1:033029.
[11] Das K, Agarwal A. Linear magnetochiral transport in tilted type-I and type-II Weyl semimetals. Phys Rev B 2019;99:085405.
[12] Sonowal K, Singh A, Agarwal A. Giant optical activity and Kerr effect in type-I and type-II Weyl semimetals. Phys Rev B 2019;100:085436.
[13] Soluyanov AA, Gresch D, Wang Z, et al. Type-II Weyl semimetals. Nature 2015;527:495–8.
[14] Zhang QR, Zeng B, Chiu YC, et al. Possible manifestations of the chiral anomaly and evidence for a magnetic field induced topological phase transition in the type-I Weyl semimetal TaAs. Phys Rev B 2019;100:115138.
[15] Yang B, Guo Q, Tremain B, et al. Ideal Weyl points and helicoid surface states in artificial photonic crystal structures. Science 2018;359:1013–6.
[16] Lv B, Qian T, Ding H. Angle-resolved photoemission spectroscopy and its application to topological materials. Nat Rev Phys 2019;1:609–26.
[17] Zheng H, Hasan MZ. Quasiparticle interference on type-I and type-II Weyl semimetal surfaces: a review. Adv Phys: X 2018;3:1466661.
[18] Li P, Wen Y, He X, et al. Evidence for topological type-II Weyl semimetal WTe_2. Nat Commun 2017;8:2150.
[19] Xu S-Y, Alidoust N, Chang G, et al. Discovery of Lorentz-violating type II Weyl fermions in LaAlGe. Sci Adv 2017;3:e1603266.
[20] Yao M-Y, Xu N, Wu QS, et al. Observation of Weyl nodes in robust type-II Weyl semimetal WP_2. Phys Rev Lett 2019;122:176402.
[21] Zyuzina AA, Tiwari RP. Intrinsic anomalous Hall effect in type-II Weyl semimetals. JETP Lett 2016;103:717–22.
[22] Rostamzadeh S, Adagideli I, Goerbig MO. Large enhancement of conductivity in Weyl semimetals with tilted cones: pseudorelativity and linear response. Phys Rev B 2019;100:075438.
[23] Lin H, Chen B, Yang S, et al. Photonic spin Hall effect of monolayer black phosphorus in the Terahertz region. Nanophotonics 2018;7:1929–37.
[24] Liu Y, Ke Y, Luo H, Wen S. Photonic spin Hall effect in metasurfaces: a brief review. Nanophotonics 2017;6:51–70.
[25] Nalitov AV, Malpuech G, Terças H, Solnyshkov DD. Spin-orbit coupling and the optical spin Hall effect in photonic graphene. Phys Rev Lett 2015;114:026803.
[26] Zhou X, Lin X, Xiao Z, et al. Controlling photonic spin Hall effect via exceptional points. Phys Rev B 2019;100:115429.
[27] Onoda M, Murakami S, Nagaosa N. Hall effect of light. Phys Rev Lett 2004;93:083901.
[28] Hosten O, Kwiat P. Observation of the spin Hall effect of light via weak measurements. Science 2008;319:787–90.
[29] Ye W, Liu Y, Liu J, Horsley SAR, Wen S, Zhang S. Photonic Hall effect and helical Zitterbewegung in a synthetic Weyl system. Light Sci Appl 2019;8:49.
[30] Chen S, Mi C, Wu W, et al. Weak-value amplification for Weyl-point separation in momentum space. New J Phys 2018;20:103050.
[31] Kort-Kamp WJM. Topological phase transitions in the photonic spin Hall effect. Phys Rev Lett 2017;119:147401.
[32] Li J, Tang T, Luo L, Yao J. Enhancement and modulation of photonic spin Hall effect by defect modes in photonic crystals with graphene. Carbon 2018;134:293–300.
[33] Ye G, Zhang W, Wu W, et al. Goos-Hänchen and Imbert-Fedorov effects in Weyl semimetals. Phys Rev A 2019;99:023807.
[34] Naidyuk YG, Bashlakov DL, Kvitnitskaya OE, et al. Yanson point-contact spectroscopy of Weyl semimetal WTe_2. 2D Mater 2019;6:045012.
[35] Ahn S, Mele EJ, Min H. Optical conductivity of multi-Weyl semimetals. Phys Rev B 2017;95:161112(R).
[36] Kargarian M, Randeria M, Trivedi N. Theory of Kerr and Faraday rotations and linear dichroism in topological Weyl semimetals. Sci Rep 2015;5:12683.
[37] Son YW. Topological properties controlled by light. Nature 2019;565:32–3.
[38] Liu ZK, Yang LX, Sun Y, et al. Evolution of the Fermi surface of Weyl semimetals in the transition metal pnictide family. Nat Mater 2016;15:27–31.
[39] Zhang W, Wu W, Chen S, et al. Photonic spin Hall effect on the surface of anisotropic two-dimensional atomic crystals. Photonics Res 2018;6:511–6.
[40] Jia G, Li G, Zhou Y, et al. Landau quantisation of photonic spin Hall effect in monolayer black phosphorus. Nanophotonics 2020;9:225–33.

Supplementary Material: The online version of this article offers supplementary material (https://doi.org/10.1515/nanoph-2019-0468).